JACS
JOURNAL OF THE AMERICAN CHEMICAL SOCIETY
Article
pubs.acs.org/JACS

Composition and Structure of the Inorganic Core of Relaxed Intermediate X(Y122F) of *Escherichia coli* Ribonucleotide Reductase

Peter E. Doan,*[,†] Muralidharan Shanmugam,[‡] JoAnne Stubbe,*[,§] and Brian M. Hoffman*[,†]

[†]Department of Chemistry, Northwestern University, Evanston, Illinois 60208-3113, United States
[‡]Manchester Institute of Biotechnology, The University of Manchester, Manchester M1 7DN, United Kingdom
[§]Department of Chemistry, Massachusetts Institute of Technology, Cambridge, Massachusetts 02139-4307, United States

Supporting Information

ABSTRACT: Activation of the diferrous center of the β2 (R2) subunit of the class 1a *Escherichia coli* ribonucleotide reductases by reaction with O_2 followed by one-electron reduction yields a spin-coupled, paramagnetic Fe(III)/Fe(IV) intermediate, denoted **X**, whose identity has been sought by multiple investigators for over a quarter of a century. To determine the composition and structure of **X**, the present study has applied ^{57}Fe, ^{14,15}N, ^{17}O, and ^{1}H electron nuclear double resonance (ENDOR) measurements combined with quantitative measurements of ^{17}O and ^{1}H electron paramagnetic resonance line-broadening studies to wild-type **X**, which is very short-lived, and to **X** prepared with the Y122F mutant, which has a lifetime of many seconds. Previous studies have established that over several seconds the as-formed **X**(Y122F) relaxes to an equilibrium structure. The present study focuses on the relaxed structure. It establishes that the inorganic core of relaxed **X** has the composition [$(OH^-)Fe^{III}$–O–Fe^{IV}]: there is *no* second inorganic oxygenic bridge, neither oxo nor hydroxo. Geometric analysis of the ^{14}N ENDOR data, together with recent extended X-ray absorption fine structure measurements of the Fe–Fe distance (Dassama, L. M.; et al. *J. Am. Chem. Soc.* **2013**, 135, 16758), supports the view that **X** contains a "diamond-core" Fe(III)/Fe(IV) center, with the irons bridged by two ligands. One bridging ligand is the oxo bridge (O_{Br}) derived from O_2 gas. Given the absence of a second inorganic oxygenic bridge, the second bridging ligand must be protein derived, and is most plausibly assigned as a carboxyl oxygen from E238.

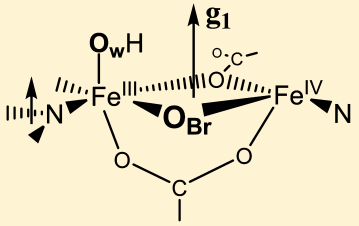

1. INTRODUCTION

The β2 (R2) subunit of the class 1a *Escherichia coli* ribonucleotide reductases (RNRs) is one of the class of diferrous nonheme iron proteins that carry out a broad range of reactions, ranging from reversible O_2 binding to fatty acid desaturation and methane oxidation.[1−4] The RNRs catalyze the conversion of nucleoside diphosphates to deoxynucleoside diphosphates in reactions involving complex free radical chemistry.[5−7] The β2 subunits in their oxidized forms/states contain a nonheme diferric center adjacent to a tyrosyl radical ($Y^{\bullet}$)[8,9] that initiates the reduction process. The active diferric–$Y^{\bullet}$ cofactor in vitro is generated from the diferrous–Y center in a reaction with O_2 and an external reductant. This process has been studied by a number of time-resolved biophysical methods, including stopped-flow and rapid freeze-quench (RFQ) electron paramagnetic resonance (EPR), electron nuclear double resonance (ENDOR), Mössbauer, magnetic circular dichroism (MCD), and extended X-ray absorption fine structure (EXAFS) spectroscopies.[10−16] A paramagnetic diiron intermediate designated **X** has been observed by all of these methods. **X** is one-electron-oxidized relative to the resting diferric state of β2 and is catalytically competent to oxidize tyrosine 122 to $Y122^{\bullet}$.[17,18] RFQ Q-band ^{57}Fe ENDOR spectroscopy[19] established that the diiron center of **X** has an antiferromagnetically spin-coupled [Fe(III), $S = 5/2$]/[Fe(IV), $S = 2$] core with an $S = 1/2$ ground state. As **X** both is the first high-valent intermediate of a diiron center to be trapped and can be readily trapped in high yield, it has been the paradigm for such reactive states for over a quarter of a century. Nonetheless, to date no consensus has been reached as to the composition and structure of **X**.

Studies of many diiron proteins, in different oxidation states, indicate that the observed antiferromagnetic exchange coupling between the Fe ions of **X** requires the presence of one or more oxo and/or hydroxo bridges. Some time ago we used a combination of ^{1}H and ^{2}H, ^{17}O continuous-wave (CW) and pulsed ENDOR protocols to identify the inorganic core of **X**: the number of oxo bridges and the types of protonated oxygen (OH_x) species and their disposition relative to the ferric and ferryl ions of **X**.[12,14,20] These studies led us to conclude that the [$(H_xO)Fe^{III}$–O–Fe^{IV}] fragment forms the complete inorganic core of **X**, with the possibility that additional bridging ligand(s) supplied by the protein complete the core structure.

This interpretation was subsequently questioned by computational studies whose efforts were driven by the EXAFS measurement of an Fe–Fe distance of 2.51 Å,[11] which was viewed as being too short to be compatible with our proposal. One of these studies proposed that **X** has a μ-oxo/μ-hydroxo-Fe(III)/Fe(IV) core, but did not address the existence of terminal H_xO,[10] and the other study[21,22] concluded that **X** possesses a di-μ-oxo-Fe(III)/Fe(IV) core plus a terminal H_2O

Received: October 14, 2015
Published: December 4, 2015

DOI: 10.1021/jacs.5b10763
J. Am. Chem. Soc. 2015, 137, 15558−15566

bound to the Fe(III) ion.[22] Thus, each of the two studies includes features that differ from our proposed structure, but they do not agree between themselves. As a first step toward resolving the issue, we took advantage of improvements in the 35 GHz pulsed ENDOR performance to reexamine the protonation state of the oxygenic ligands of the inorganic core of **X** by *directly* probing the exchangeable proton(s) with ^{2}H pulsed ENDOR spectroscopy. This study confirmed (i) that **X** contains a terminal OH_x ligand to the Fe(III) ion and (ii) that **X** does not contain a μ-hydroxo bridge.[23] A very recent EXAFS study of **X** has proposed a greater Fe−Fe distance, 2.78 Å, but nonetheless suggested the present of a di-μ-oxo-Fe(III)/Fe(IV) core.[24]

In the present study we definitively answer the question of the number of ^{17}O atoms from $^{17}O_2$ incorporated in **X** by combining Q-band pulsed ENDOR measurements of the ^{17}O hyperfine couplings with quantitative measurements of ^{17}O EPR line broadening that utilize the couplings. We further establish that the solvent-derived OH_x aqua ligand of Fe(III) is a hydroxo (x = 1) derived from solvent, and determine that a second atom of ^{17}O is not incorporated from solvent. These findings complete the assignment of the inorganic core of X.

In carrying out this effort, we explicitly address issues associated with the nature of the RNR samples used by us and others in spectroscopic studies. First, **X** in wild-type (WT) RNR is formed so rapidly that the tyrosyl radical is generated even at the earliest time points, and this interferes with the analyses, so measurements are generally made with the stable **X** of the Y122F-β2 variant. Second, ^{17}O hyperfine EPR broadening and ENDOR of **X**(Y122F) reveal that the second atom of $^{17}O_2$ is lost as the RFQ delay time is extended from 8 ms to several seconds and **X** relaxes to its equilibrium structure.[14] We here use ^{57}Fe, ^{14,15}N Q-band pulsed ENDOR measurements to show that the [Fe_2, His_2] coordination center of **X** is unchanged by the Y122F mutation and is invariant with the quench delay time, despite the relaxation process, and that the OH^- ligand is fully occupied throughout the process. We further report minor perturbations to the H_xO coordinated to the Fe(III) ion caused by the loss of a putative H-bond with the Y122 hydroxyl mediated by D84. Finally, as the conclusion to a quarter of a century of studies by many investigators, the measurements of ^{17}O ENDOR and EPR line broadening definitively yield the composition and give a most probable structure for the inorganic core of **X**(Y122F) that has relaxed to its final, equilibrium structure.

2. MATERIALS AND METHODS

2.1. Samples. **X** in WT β2 and Y122F-β2 in D_2O buffer was prepared by RFQ methods as reported,[14] and stored in liquid nitrogen. EPR and ENDOR (35 GHz) spectroscopies demonstrate that the signals are unchanged by this storage.

2.2. ENDOR Spectroscopy. The 35 GHz pulsed ENDOR spectrometer[25] employed in this study has been described.[26] As discussed in detail,[27−29] for a frozen solution sample, the determination of the full hyperfine tensor (and quadrupole tensor) of an interacting nucleus is achieved by obtaining a 2-D set of orientation-selective ENDOR spectra collected at multiple fields across the EPR envelope and comparing this set with simulated 2-D patterns. The ENDOR simulations were performed with the program Endorsim, an enhanced version of the simulation program GENDOR.[27] The Davies and Mims response factors have a major influence on the observed ENDOR response, and are incorporated into Endorsim.[27]

3. RESULTS AND DISCUSSION

3.1. Spin Coupling and the Spin Hamiltonian Parameters of X. The EPR spectra taken of **X** prepared with the WT and mutant (Y122F) RNRs preloaded with Fe(II), mixed with O_2-saturated buffer, and freeze-quenched in isopentane[14] 42 ms after mixing, as well as relaxed **X**(Y122F) quenched at 4 s, all have the same **g**-tensor, whose values we find to be g = [2.006, 1.998, 1.993]. This **g**-tensor is almost perfectly rhombic, but the deviations from this limit leave g_1 as the unique magnetic direction. The **g**-tensor of an antiferromagnetically spin-coupled [Fe(III), S = 5/2]/[Fe(IV), S = 2] diiron center such as **X** is described by the following equation:[30]

$$\mathbf{g} = K(\mathrm{III}) \times \mathbf{g}(\mathrm{Fe(III)}) + K(\mathrm{IV}) \times \mathbf{g}(\mathrm{Fe(IV)})$$
$$K(\mathrm{III}) = 7/3 \qquad K(\mathrm{IV}) = -4/3 \tag{1}$$

where the $K(i)$ are vector-coupling projection coefficients arising from the exchange coupling.

The Fe(III) ion **g**-tensor, **g**(Fe(III)), is essentially isotropic, so the anisotropy of **g** is determined by that of the Fe(IV) ion **g**-tensor, **g**(Fe(IV)). In general, the unique direction of this single-ion **g**-tensor, and thus **g** for the coupled center, corresponds to the direction of the axial component of the zero-field splitting tensor associated with the S = 2 Fe(IV) ion. This in turn is oriented along the direction of the strongest rhombic ligand-field component, which corresponds to the strongest bond to the Fe(IV) ion. We interpret the invariant g-values as evidence that the ligand field at Fe(IV), and thus the coordination sphere of this ion, is not perturbed by the Y122F mutation, and does not change significantly at 4 s after formation. We return to this issue below through ENDOR measurements of the hyperfine couplings to the ^{57}Fe(i) and coordinated ligands, in particular histidyl ^{14}N nitrogens.

For use below, we further note that the hyperfine coupling tensor observed for a nucleus (n), **A**(n), of a ligand bound to one of the Fe ions, Fe(i), i = III or IV, equals the product of its single-ion hyperfine coupling, **A**(n,i), as determined by the bonding to Fe(i), multiplied by the Fe(i) vector-coupling projection coefficient:

$$\mathbf{A}(\mathrm{n}) = K(i) \times \mathbf{A}(\mathrm{n}, i) \tag{2a}$$

When the ligand interacts with both Fe ions, as would for example occur for an atom associated with a bridge, its observed hyperfine tensor is given by the sum of the intrinsic couplings to each iron, as weighted by the corresponding vector-coupling projection coefficient:

$$\mathbf{A}(n) = K(\mathrm{III}) \times \mathbf{A}(\mathrm{n, III}) + K(\mathrm{IV}) \times \mathbf{A}(\mathrm{n, IV})$$
$$= 7/3 \times \mathbf{A}(\mathrm{n, III}) - 4/3 \times \mathbf{A}(\mathrm{n, IV}) \tag{2b}$$

3.2. ^{57}Fe and ^{14}N ENDOR Spectra of X(WT/Y122F). In this section we use a variety of double resonance/magnetic resonance techniques to characterize the ^{57}Fe ions of **X** and their histidyl ^{14}N ligands. We show that their magnetic properties are unchanged by the Y122F mutation and invariant to the delay time before the samples are freeze-quenched after mixing with O_2-saturated buffer.

3.2.1. ^{57}Fe Davies ENDOR. Figure 1 compares the 2-D field-frequency patterns of Davies ENDOR spectra collected across the EPR envelope of ^{57}Fe-enriched **X**(Y122F) freeze-quenched at 8 ms and 4 s delay times after mixing, and Figure S1A compares patterns for **X**(WT) and **X**(Y122F) freeze-quenched

DOI: 10.1021/jacs.5b10763
J. Am. Chem. Soc. 2015, 137, 15558−15566

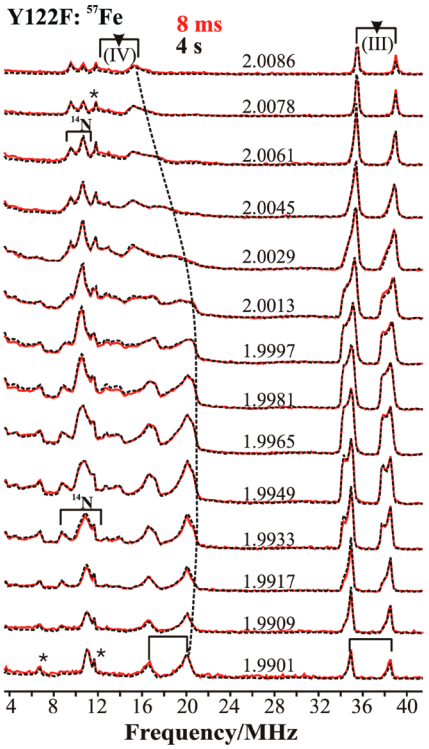

Figure 1. 2-D field-frequency plot of Davies ^{57}Fe ENDOR spectra of **X**(Y122F) prepared with ^{57}Fe and freeze-quenched at 8 ms (red lines) and 4 s (black dotted lines) after mixing. Note that the indicated precision of the *g*-values reflects the precision of the differences in the *g*-values, which is determined by differences in the magnetic fields (10.0 G steps). Conditions: π pulse length 80 ns, τ = 600 ns, repetition time 50 ms, average microwave frequency 34.95 GHz, T = 2 K. The asterisks indicate the third harmonics of the ^{57}Fe(III) and ^{57}Fe(IV) ENDOR signals. (*g*-values represent the relative precision of five significant figures, not the absolute accuracy.)

at 42 ms (WT)/8 ms (Y122F) after mixing. Comparison of the three patterns with spectra from unenriched samples shows well-defined ^{57}Fe signals in the 34−40 and 14−22 MHz ranges, the former associated with the ^{57}Fe(III) ion and the latter with the ^{57}Fe(IV) ion. The 2-D field-frequency patterns of Figure S1B show that the mutation causes no changes in the properties of either of the Fe ions of **X**. Correspondingly, Figure 1 shows that both the Fe(III) and Fe(IV) ENDOR signals are *identical* at early and late quench times, likewise indicating that the coordination spheres of both Fe ions are invariant with the quench delay after mixing.

The 2-D ^{57}Fe(III) and ^{57}Fe(IV) patterns all are extremely well simulated (Figure S1B) with a hyperfine tensor for ^{57}Fe(III) that is nearly isotropic, $a_{iso}(^{57}Fe(III))$ = −73.5 MHz, while that for Fe(IV) is substantially anisotropic and has an isotropic component roughly half that of Fe(III), $a_{iso}(^{57}Fe(IV))$ = +33.9 MHz. The tensor values for both Fe ions (Table 1) are in good agreement with those reported previously for **X**(Y122F).[19] The signs of the isotropic couplings for the two Fe ions were obtained by raw data pulsed ENDOR saturation and recovery (RD-PESTRE) measurements (Figure S2).[31] They reflect the signs of the vector coupling projection coefficients for the spin-coupled diiron center as described in eq 2a.

Both the **g**-tensor and the orientation of the ^{57}Fe(IV) hyperfine tensor are determined by the zero-field tensor at ^{57}Fe(IV). As reported previously for the Y122F mutant quenched at 600 ms,[19] within error, the **A**-tensor of ^{57}Fe(IV) and **g**-tensor are coaxial. As would thus be expected, the unique value of the Fe(IV) hyperfine tensor is associated with the unique *g*-value, g_1, both being assignable to the direction of the principal component of the zero-field splitting tensor.

3.2.2. ^{14}N Davies ENDOR. The ^{14}N Davies ENDOR responses from the histidyl ^{14}N coordinated to Fe(III) (denoted $^{14}N(III)_C$) of **X** appear in the 6−14 MHz region of Figure 1 and in Figures 2 and S1. As is the case with the ^{57}Fe ENDOR spectra, the ^{14}N Davies ENDOR spectra of **X**(WT) and **X**(Y122F) collected at 42 ms (WT)/8 ms(Y122F) and of **X**(Y122F) at 8 ms and 4 s are *identical*, Figures 1 and S1A. Analysis of the 2-D field-frequency pattern of ^{14}N Davies ENDOR spectra (Figure 2) gives the modestly anisotropic $^{14}N(III)_C$ coupling tensor, $\mathbf{A}(^{14}N(III)_C)$ = [12.8, 11.8, 17.1] MHz, $a_{iso}(^{14}N(III)_C)$ = 13.9 MHz, and a quadrupole interaction tensor typical of Fe-bound histidine ^{14}N, **P** = [−0.40, −0.73, +1.13] MHz. The positive sign of the hyperfine coupling for $^{14}N(III)_C$ was obtained by RD-PESTRE measurements (Figure S2). The two tensors are coaxial, with the A_1 and $P_1 = P_x$ directions (defined by $|P_x| < |P_y| < |P_z|$) closely parallel with g_1 (Table 1). Numerous studies of the high-spin Fe-bound ^{14}N of histidine show that these maximum hyperfine and nuclear-quadrupole interactions lie along the ^{14}N−Fe(III) bond vector, whereas the minimum quadrupole interaction (P_x) is normal to the imidazole plane.[32] Therefore, the measurements show that g_1 lies roughly normal to the plane of the imidazole bound to the Fe(III) ion.

3.2.3. $^{14/15}$N Mims ENDOR. Mims ENDOR spectra of ^{14}N associated with the more weakly coupled histidine bound to Fe(IV) (denoted $^{14}N(IV)_C$) are poorly resolved (not shown). However, Figure 3 shows the well-resolved ^{15}N Mims ENDOR response of $^{14}N(IV)_C$, as well as a signal from the remote ^{15}N of the histidine bound to Fe(III) (denoted $^{15}N(III)_R$). Both ^{15}N nuclei have hyperfine interaction (HFI) dominated by an

Table 1. Hyperfine Interactions of Relaxed RNR Intermediate X

	RNR-X								
	$^{17}O_w$		$^{17}O_{Br}$	^{57}Fe(IV)	^{57}Fe(III)	$^{14}N(III)_C$ [b]		$^{14}N(III)_R$ [c]	$^{14}N(IV)_C$ [c]
hyperfine coupling (MHz)	A	P	A	A	A	A	P	A	A
A_1	−34.1	0.07	[5][a]	+26.3	−74.8	+12.8	−0.40	0.58	
A_2	−23.6	−0.38	−21.4	+38.4	−72.0	+11.8	−0.73	1.04	
A_3	−18.6	0.31	−21.4	+37.1	−73.7	+17.1	+1.13	0.66	
a_{iso}	−25.4		[−12.6][a]	+33.9	−73.5	+13.9		0.76	~1.4

[a]Estimated. [b]Tensors coaxial. Euler angles [α = 0°, β = 6°, γ = 51°] as previously defined.[36,37] [c]Calculated from parameters for the ^{15}N isotopomer by scaling with the ratio of nuclear *g*-factors.

DOI: 10.1021/jacs.5b10763
J. Am. Chem. Soc. 2015, 137, 15558−15566

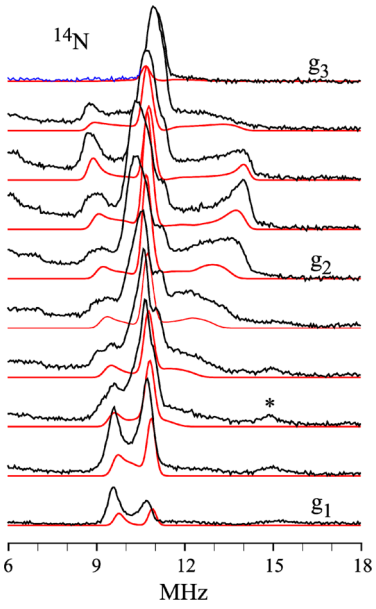

Figure 2. (Black) Davies ENDOR spectra of the $^{14}N_{Im}$ coordinated to the Fe(III) ion for RNR **X** taken at 10.0 G intervals across the EPR envelope of **X**(Y122F). The asterisk indicates the feature in the vicinity of 15 MHz that appears as g approaches g_1 is a proton harmonic. (Red) Simulations using hyperfine and quadrupole parameters given in Table 1.

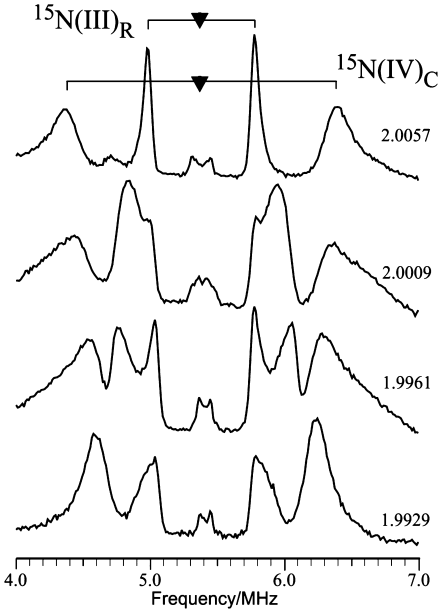

Figure 3. Mims ENDOR spectra of weakly coupled ^{15}N nuclei in globally labeled ^{15}N **X**(Y122F) freeze-quenched at 620 ms after mixing. Two patterns from distinct sites are apparent. The broader outer peaks are assigned to the coordinated N_δ-His on the Fe(IV) ion; it is characterized by a predominantly isotropic HFI with $a_{iso}(^{15}N) \approx$ 2.0 MHz. The narrower inner peaks are associated with the remote ^{15}N of the histidine imidazole coordinated to the Fe(III) ion. Conditions: microwave frequency 35.04 GHz, τ = 250 ns, T_{RF} = 40 us, T = 2 K. (g-values represent the relative precision of five significant figures, not the absolute accuracy.)

isotropic component, but the signal from $^{15}N(IV)_C$ is relatively broad (around 0.3 MHz full width at half-maximum) when compared to the hyperfine interaction (around 2 MHz). Typically ^{15}N line widths scale with the isotropic coupling, but the line width of the coordinated Fe(IV) His, $^{15}N(IV)c$, is approximately the same as that associated with $^{15}N(III)c$, whose isotropic coupling is approximately 10× larger. This suggests that the coordination geometry of $^{14,15}N(IV)c$ is not sharply defined. Indeed, the anisotropy of this hyperfine interaction is less than the line width, making detailed analysis impossible.

In contrast to these broad lines, the narrow features (ca. 0.070 MHz) associated with $^{15}N(III)_R$ allow for a straightforward analysis of its tensor components with $|\mathbf{A}(^{15}N(III)_R)|$ = (0.81, 1.45, 0.92) MHz.

3.2.4. Conclusions from ^{57}Fe and ^{14}N ENDOR. The ^{57}Fe ENDOR spectra of **X**(WT) quenched at 42 ms and **X**(Y122F) quenched at 8 ms and 4 s all are identical. The same is true for the ^{14}N ENDOR spectra. In particular, the hyperfine and quadrupole interactions of the histidine bound to the Fe(III) ion are invariant.

The unique value of the Fe(IV) hyperfine tensor is oriented along the unique g-value, g_1, which corresponds to the principal direction of the zero-field splitting tensor. The orientation of the hyperfine and quadrupole tensors of $^{14}N(III)_C$ shows that the Fe(III)−N bond lies in the g_2−g_3 plane, perpendicular to g_1, and that the normal to the plane of the histidine imidazole is closely parallel to g_1.

3.3. Fe(III)-Bound $^{17}O_wH_x$. In this section we recall the results of recent ^{1,2}H ENDOR studies of **X** and describe the present use of quantitative EPR measurements of **X** in H_2O/D_2O to determine the protonation state, "x", of an Fe(III)-bound OH_x. We further report the present use of multiple magnetic resonance/double resonance techniques to characterize the solvent-derived $^{17}OH_x$ ligand. In this one instance we compare the properties of the oxygen of this ligand, denoted $^{17}O_w$, in the WT enzyme quenched at 42 ms with that of the mutant enzyme quenched at 42 ms and 4 s to test our previous suggestion that the $^{17}OH_x$ ligand changes its occupancy over the quenching delay period, 8 ms to 4 s.

3.3.1. ^{1,2}H ENDOR, EPR, and Characterization of the Protonated Oxygenic Ligands of X. We recall the following definitive results of our recent study of the protonation state of oxygenic ligands of the inorganic core of **X**.[23] By directly probing the exchangeable proton(s) with ^{2}H pulsed ENDOR spectroscopy, these measurements confirmed that **X** contains an Fe(III)-bound terminal aqua ligand (H_xO), and does *not* contain a μ-hydroxo bridge. The ^{2}H ENDOR measurements further demonstrated that this conclusion is applicable to both the wild type and the β2 Y122F mutant; in fact, we detected *no* difference between the properties of protons on the terminal oxygens in the two variants.

The ^{2}H ENDOR spectra collected from the OH_x aqua ligand were accurately simulated with a single ^{2}H bound to the ligand with a single orientation, and thus are most plausibly assigned to a terminal hydroxyl (OD^-). The only way the ^{1,2}H ENDOR results would be consistent with a water ligand, x = 2, would be if the two protons were related by a symmetry element, a 2-fold axis running along the Fe−O vector, or a mirror plane with Fe−O lying in that plane. Given the unsymmetric environment of the aqua ligand on Fe1, this seems highly unlikely.

To test this proposal, that is, that x = 1, we have now compared the X-band EPR spectra of RNR **X**(Y122F) quenched in H_2O and D_2O at 4 s to see if this could confirm the presence of a hydroxide ligand (x = 1 proton), rather than a water ligand (x = 2) on the Fe(III) ion. As shown in Figure S3,

DOI: 10.1021/jacs.5b10763
J. Am. Chem. Soc. 2015, 137, 15558−15566

only $x = 1$ gives a satisfactory description of the broadening of the EPR envelope of **X** in H_2O buffer relative to the envelope of the intermediate in D_2O buffer. Thus, the ENDOR and EPR hyperfine broadening measurements agree that the solvent-derived OH_x ligand on Fe(III) in **X** is a hydroxo ligand: $x = 1$.

3.3.2. $^{17}O_w$ at 42 ms. Figure 4 presents 35 GHz Davies ^{17}O ENDOR spectra recorded at the three canonical g-values for

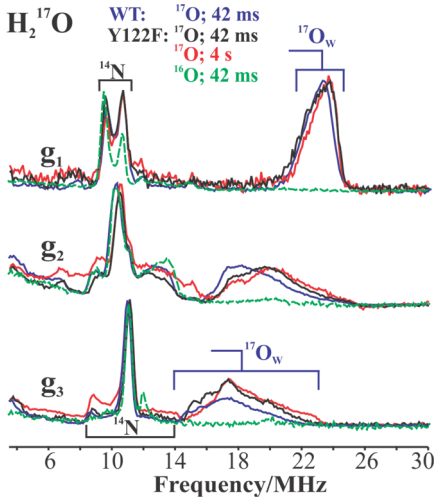

Figure 4. Davies pulsed ENDOR spectra of $^{17}O_w$ in **X** at the three canonical g-values, prepared with $^{17}OH_2$ buffer: Y122F freeze-quenched at 42 ms (black) and 4 s (red) after mixing; WT freeze-quenched at 42 ms (blue). As the baseline, a spectrum is included for the abundance of **X**(Y122F) (green) (42 ms) prepared in natural-abundance buffer solution. Conditions: π pulse length 80 ns, τ = 600 ns, repetition time 50 ms, 34.971 GHz (Y122F), 34.93 GHz (WT), T = 2 K.

X(WT) and **X**(Y122F) prepared with $H_2{}^{17}O$ and quenched at 42 ms, and also at 4 s for Y122F. In addition to the strong ^{14}N ENDOR responses in the 6−16 MHz range (described above), the spectrum of **X**(WT) prepared in $H_2{}^{17}O$ buffer and collected at g_1 displays an additional intense feature assigned as the ν_+ branch of the solvent-derived oxygen associated with the core of **X**, denoted $^{17}O_w$ and previously assigned as an $^{17}O_wH$ ligand bound to Fe(III) of **X**. The peak is centered at $\nu_+ = A(^{17}O_w)/2 + \nu(^{17}O) \approx 24$ MHz, corresponding to a hyperfine coupling of $A(^{17}O_w) \approx 34$ MHz, and is broadened by a small, unresolved quadrupole interaction, $12P_1 \approx 4-5$ MHz (Figure 4). As the field is increased toward g_2 and g_3, the ^{17}O ENDOR response shifts to lower frequency, at g_3 becoming a broad feature centered at $\nu_+ \approx 18$ MHz ($A(^{17}O_w) \approx 19$ MHz) and exhibiting a large unresolved quadrupole splitting, $12P_3 \approx 7-8$ MHz.

The entire 2-D pattern of Davies pulsed $^{17}O_w$ ENDOR spectra collected over the EPR envelope is shown in Figure S4, and is in excellent agreement with the CW ENDOR measurements reported earlier for **X**(Y122F).[14] As illustrated in the spectra taken at the canonical g-values, g_1, g_2, and g_3 shown in Figure 4, the $^{17}O_w$ ENDOR responses are so alike that they correspond to essentially identical couplings for **X**(WT) (blue), relaxed **X**(Y122F) (red), and even **X**(Y122F) collected at early time (black). The spectra in Figure 4 show only subtle differences in the shapes at g_2 and g_3 of $^{17}O_w$ ENDOR spectra of **X**(WT) from those of the two **X**(Y122F) preparations, best resolved at the g_3 single-crystal-like field. This difference is likely due to the loss of H-bonding interaction between the $[^{17}O_wH]^-$ ligand and the OH of Y122 through the D84 ligand to the Fe(III) ion and its absence in the mutant, but as discussed immediately below, the hyperfine tensor for $^{17}O_w$ (Y122F) is the same as that of $^{17}O_w$ (WT) within error (Table 1).

The experimental patterns of Davies pulsed $^{17}O_w$ ENDOR spectra for **X**(Y122F) and **X**(WT) were both well simulated (not shown) by assuming a single contributing $^{17}O_w$ with the hyperfine tensor, $\mathbf{A}(^{17}O_w) = -[34, 24, 19]$ MHz, dominated by an isotropic coupling of $a_{iso}(^{17}O_w) = -25.4$ MHz (see Table 1 for other parameters). In the absence of a successful direct measurement of the sign of the coupling to $^{17}O_w$, the signs of the HFI were assigned by assuming positive spin density on $^{17}O_w$ derived from direct delocalization from the Fe(III) ion; as $g_N < 0$ for ^{17}O and we assume $\rho(O_w) \approx A/g_N > 0$, then $A(^{17}O_w) < 0$. The derived couplings match the values reported for $^{17}O_w$ (Y122F) by Burdi et al., within error.[14]

3.3.3. $^{17}O_w$ ENDOR, 4 s vs 42 ms. Comparison of the 35 GHz 2-D field-frequency Davies pulsed ENDOR patterns for **X**(Y122F) samples prepared in $H_2{}^{17}O$ buffer and quenched early (42 ms; black) and late (4 s; red), Figure 4, clearly shows the frequencies of the $^{17}O_w$ ENDOR features observed at short and long quenching times are identical, and thus, the properties of $^{17}O_w$ as indicated by its spin Hamiltonian parameters do not change during delay before quenching. Of particular significance, normalization of each of the current Davies ENDOR spectra to its ^{14}N signal as an internal reference, and comparison of the intensities of the normalized spectra from **X** quenched at 42 ms and 4 s, shows that the intensity of the $^{17}O_w$ signal does *not* change as the quench time is lengthened from 42 ms to 4 s, Figure 4. This observation corrects the interpretation of our earlier measurements[14] that the intensity of the signal from $^{17}O_w$ does exhibit a change, with $^{17}O_w$ "exchanging in" from the solvent over time. Re-examination of the earlier data[14] shows that the apparent change in intensity with time reflects subtle baseline uncertainties in the CW ENDOR measurements then employed, which are absent in the Davies pulsed ENDOR measurements.

As confirmation of the invariance of the occupancy of $H_x{}^{17}O_w$ with the quench time, Figure S5 shows ^1H ENDOR measurements that also indicate that by the earliest quench times, 8−42 ms, **X** contains an H_xO ligand that is equilibrated with solvent, and that its occupancy, properties, and isotopic composition are invariant with the quench time.

3.3.4. EPR Quantitation of $^{17}O_w$. To confirm the invariant $^{17}O_w$ site occupancy, we used the refined $^{17}O_w$ tensor values obtained here to simulate the EPR spectrum of **X** prepared in a 30% $H_2{}^{17}O$ sample and quenched at 42 ms as the sum of the individual contributions of ^{17}O and ^{16}O isotopologues. In the EPR simulations, the only adjustable parameter was the percentage occupancy of $^{17}O_w$; the g-values and ^{17}O and ^{57}Fe hyperfine tensors were fixed, and the line widths (LWs) were fixed to those derived through simulation of the spectrum of **X** prepared in $H_2{}^{16}O$. The resulting one-parameter least-squares fit yielded the EPR simulation, shown in Figure 5, in which the occupancy of $^{17}O_w$ is 30(2)%, equal to the $^{17}O_w$ percentage in the solvent. This result incidentally shows that there is no scrambling of the oxygen of the OH ligand to the Fe(III) ion with O atoms derived from $O_2(g)$ during assembly of the **X** intermediate state.

The sensitivity of these simulations to the isotopic composition is highlighted by the finding that to achieve an adequate simulation required the inclusion of contributions

DOI: 10.1021/jacs.5b10763
J. Am. Chem. Soc. 2015, 137, 15558−15566

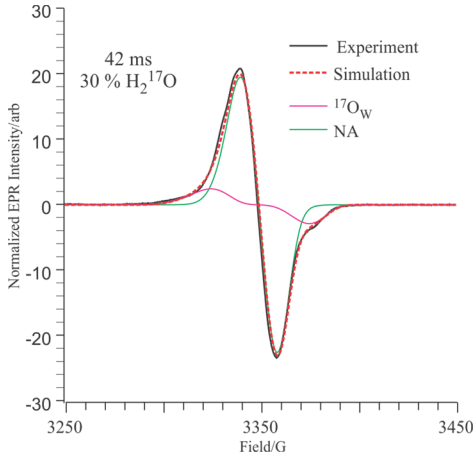

Figure 5. Normalized EPR spectrum (black solid line) and simulation (red dotted line) of **X**(Y122F) quenched at 42 ms in the presence of 30% $H_2{}^{17}O$. The simulation is the sum of 69.2% natural-abundance (green) and 30.8% $H_2{}^{17}O$ (magenta) **X**(Y122F). Experimental parameters: temperature 35.0 K, microwave power 10.0 mW, microwave frequency 9.375 GHz, modulation amplitude 4.0 G, time constant 32 ms, scan time 60 s, average of 40 scans. Simulation parameters: g = (2.0058, 2.0005, 1.9955), LW = (14, 10, 10) G, $A(^{14}N)$ = (12, 12, 17) MHz, $A(^{1}H)$ = (20, −10, −10) MHz, $A(^{57}Fe(III))$ = (75, 75, 75) MHz (weight 2.0%), $A(^{57}Fe(IV))$ = (26, 38, 38) MHz (weight 2.0%), $A(^{17}O)$ = (30, 20, 20) MHz (weight 30.0%).

from natural-abundance ^{57}Fe (2.15%) isotopologues for both the Fe(III) and Fe(IV) sites. The fit without ^{57}Fe inclusion resulted in a 2% increase in the predicted occupancy of $^{17}O_w$.

3.4. Geometric Analysis of the ^{57}Fe(IV), ^{14}N, and $^{1,2}H_2{}^{17}O_w$ Interaction Tensors. It is typically folly to attempt to analyze the spin Hamiltonian ENDOR parameters of a spin-coupled center such as **X** in terms of geometric structure without independent constraints. The magnitudes of hyperfine interactions as well as their relative signs are dependent on the spin-coupling parameters. Any atom that lies in the region between the two paramagnetic centers experiences dipolar coupling that arises from both centers and can be extremely difficult to decompose into single-ion effects in the absence of information on spin coupling. However, with **X**, we have hyperfine information for three well-defined sites that is related only to the properties of a single Fe ion: the protons (HFI) and oxygen (HFI, nuclear-quadrupole interaction (NQI)) of $(^{1,2}H^{17}O_w)^-$ bound to the Fe(III) ion, the ^{14}N of histidine bound to the Fe(III) ($^{14}N(III)_C$; HFI, NQI), and the ^{57}Fe of Fe(IV) (HFI). The ^{57}Fe HFI tensor of Fe(III) is equally well-defined, but is essentially isotropic and offers no geometric information.

We begin by assembling the directional information implicit in the ENDOR-derived nuclear interaction tensors: (i) Both the $^{17}O_w$ and $^{1,2}H$ of $(^{1,2}HO_w)^-$ exhibit axial HFIs with the Fe(III) ion of X, and these necessarily maximize roughly along the Fe(III)−O_w direction. According to the experiments, this direction corresponds to the direction of g_1. (ii) Previous studies show that the HFIs and NQIs of $^{14}N(III)_C$ bound to Fe(III) maximize in a direction along the Fe(III)−$N(III)_C$ bond. Experimentally, that direction lies in the g_2−g_3 plane, and thus, the Fe(III)−$N(III)_C$ bond is roughly perpendicular to the Fe(III)−OH bond vector.

A geometric interpretation of the orientations of the interaction tensors relative to the molecular framework of **X** is informed through use of the crystal structure of the Fe(III)−Fe(III) resting-state cluster as a guide, through the reliable assumption that there is little reorganization around the Fe(III) site of **X** when the partner Fe(IV) site of **X** is reduced by one electron to form the diferric resting state, and thus, the relative orientations of the histidine and water at the Fe(III) of **X** are essentially the same as in the crystallographically characterized diferric enzyme.[33,34] Figure 6 shows the relevant portion of the diferric structure.

In the diferric state of RNR, both Fe centers have coordinated aqua ligands shown in Figure 6, whereas, in **X**, only the ferric ion has an aqua ligand. Examination of the relative geometries of the N_{His}−Fe−O_w coordination for the two Fe ions in the diferric state shows that, for Fe(1), the His and H_2O ligands adopt a *cis* arrangement (∼90° angle between the Fe−O(1) and Fe−$N(III)_C$ bonds), while, for Fe(2), the His and H_2O ligands are in a *trans* geometry (∼180° angle between the bonds). The experimental finding that the Fe(III)−$N(III)_C$ bond is roughly perpendicular to the Fe(III)−OH bond are only consistent with the assignment of the Fe(1) site in the diferric state to the Fe(III) ion in X, and therefore the assignment of $^{14}N(III)_C$ to N_δ-His118. This assignment of Fe(III) to Fe(1) confirms earlier suggestions.

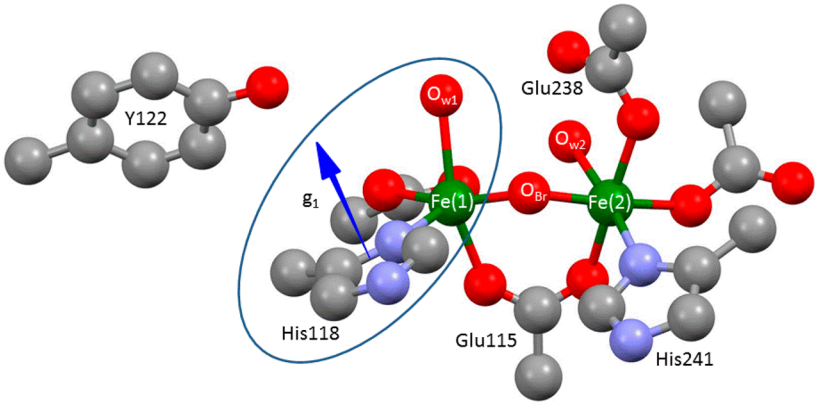

Figure 6. Structure of the diferric site from the PDB 1MXR crystal structure.[33,34] The ellipse encloses the portion of this center assumed to be a good representation of the corresponding structure of the Fe(III) site of **X**. The arrow indicates the proposed orientation of g_1. Although the **g**-tensor is fixed by the properties of the Fe(IV) ion of **X**, assigned as Fe(2), it is translated to His118 for visualization of the relative orientation of the Fe(1)−O bond.

DOI: 10.1021/jacs.5b10763
J. Am. Chem. Soc. 2015, 137, 15558−15566

It is further shown above that the normal to the plane of the His118 imidazole ligand to Fe(III) in **X** is essentially parallel to g_1 (the Fe(1)−O_w axis), and this geometry also is essentially preserved in the diferric structure at Fe(1). The fact that the relative geometries of the water and imidazole ligands of the ferric ion in **X** are maintained through the reduction of **X** to the Fe(III)−Fe(III) state is a strong indication that we can use these relationships as a guide when looking at other interactions, most notably the ^{57}Fe(IV) HFI tensor. Now consider the present finding that the unique axis of the HFI of Fe(IV) of **X** lies roughly along g_1. If we project the predicted g_1 direction onto the coordination sphere of the Fe(2) site in the diferric structure, we find that this direction is normal to the Fe−O−Fe plane of the diferric structure and roughly perpendicular to the Fe(2)−O direction, rather than being contained within the Fe−O−Fe plane. Previous studies by Solomon and co-workers[10] suggest that this arises because there is a second ligand bridging the Fe ions, with g_1 normal to the "diamond core"[35] thus formed, Chart 1. One of these bridges of course is O_{Br}; the next section discusses the identity of the second bridging ligand.

Chart 1

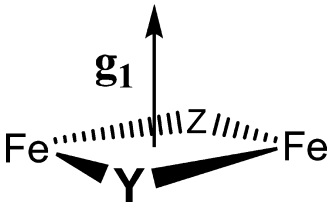

3.5. $^{17}O_2$-Derived Ligands. In this section we use pulsed ENDOR and quantitative treatment of ^{17}O hyperfine broadening to deduce the characteristics and number of ^{17}O ligands from $^{17}O_2$ that are associated with **X**(Y122F) quenched at 4 s after mixing, leading to a most probable structure for relaxed **X**.

*3.5.1. **X** Quenched at 4 s: ENDOR Measurements of $^{17}O_{Br}$.*

3.5.1.1. Davies ENDOR. In our previous study a 2-D field-frequency ENDOR pattern of ^{17}O ENDOR measurements on **X** prepared with 89% $^{17}O_2$ was generated by combining CW ENDOR spectra at high g-values with Davies ENDOR spectra at low g-values, and was interpreted as arising from a single bridging ^{17}O ligand. The improved sensitivity of the current spectrometer yielded a complete, high-quality 2-D pattern of Davies spectra, Figure 7. The spectra collected from g_3 to g_2 show a $\nu_+(^{17}O)$ feature centered at ∼18 MHz and broadened by unresolved ^{17}O quadrupole splittings. As the g-value is raised above g_2, this feature shifts to lower frequency while broadening and losing intensity, until near g_1 it is barely detectable as an apparent "rise" in the baseline. This 2-D pattern is indeed described in terms of a single ^{17}O, denoted $^{17}O_{Br}$ with $A_{\|} = A_1 \ll A_{\perp} \approx A_2 \approx A_3 \approx +21.4$ MHz. The negative sign of the coupling has been derived from RD-PESTRE measurements obtained near g_3 (Figure 8), which show that $A/g_N > 0$. As $g_N < 0$ for ^{17}O, the hyperfine sign follows; this result implies that the spin density on $^{17}O_{Br}$ is positive. Optimized values of the hyperfine and quadrupole tensor components are given in Table 1; they are in excellent agreement with those previously reported.

3.5.1.2. Site Occupancy of $^{17}O_2$-Derived Ligands Deduced from X-Band EPR Line Broadening of Y122F($^{17}O_2$). Using the ENDOR-derived HFI values for $^{17}O_{Br}$ as a guide, we have

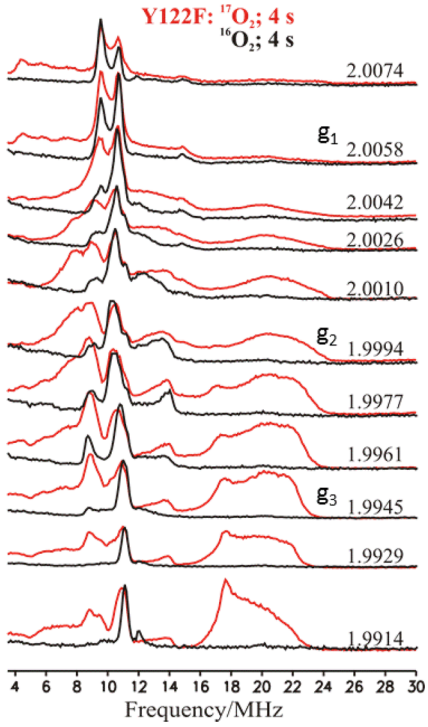

Figure 7. 2-D field-frequency plot of Davies ENDOR of **X**(Y122F) prepared with natural-abundance $^{16}O_2$ (black solid lines) and 89% $^{17}O_2$ quenched at 4 s (red solid lines). Conditions: π pulse length 80 ns, τ = 600 ns, repetition time 50 ms, T_{rf} = 40 μs, average microwave frequency 34.96 GHz, T = 2 K.

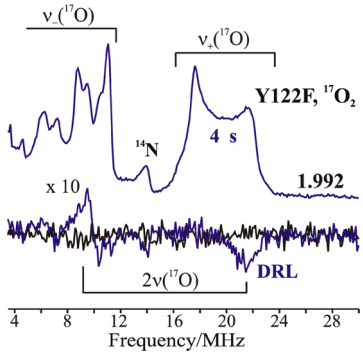

Figure 8. Top: Davies pulsed ^{17}O ENDOR spectra recorded at g_3 = 1.992 for **X**(Y122F) prepared with $^{17}O_2$ gas and freeze-quenched at 4 s (blue lines). Bottom: Corresponding ^{17}O RD-PESTRE traces (blue trace) with the null trace (black). The intensity of the RD-PESTRE spectrum is multiplied 10-fold relative to the ENDOR traces. The goalposts defined the ν_+/ν_- branches of the ^{17}O signal. Conditions: see Figure 7.

simulated the X-band EPR spectrum of the **X**(Y122F) quenched at 4 s after formation with 89% $^{17}O_2$(g). The values of A_2 and A_3 were fixed at 25 MHz, the values of A_1 and the ^{17}O occupancy were allowed to vary, and all other parameters were fixed as above. The best fit at 4 s, Figure 9, was obtained with 82% labeling of a single O_{Br} that has $|A_1| \approx 11$. Relaxing the constraint $A_2 = A_3$ improved the fit slightly, but without a significant change in occupancy. This confirms that relaxed **X**(Y122F) contains only the single $^{17}O_{Br}$ atom from $^{17}O_2$(g) with essentially complete conversion of one ^{17}O atom of the diatomic to the bridging oxo ligand. This O_2 gas derived site

DOI: 10.1021/jacs.5b10763
J. Am. Chem. Soc. 2015, 137, 15558−15566

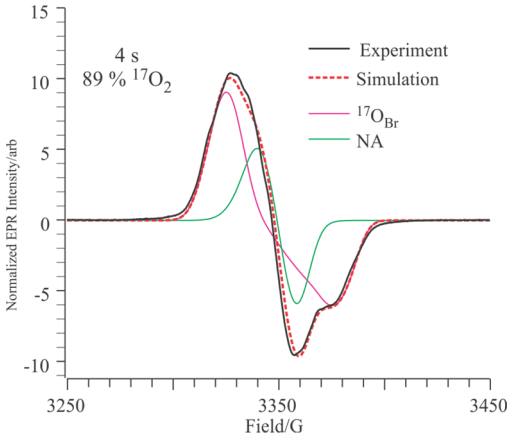

Figure 9. Normalized X-band EPR (black solid line) and simulation (red dotted line) of **X** (Y122F) quenched at 4 s in 89% $^{17}O_2$(g). The simulation is a simple sum of the green and magenta spectra, which show the decomposition into 18.0% natural-abundance $^{16}O_2$ (green) and 82% $^{17}O_{Br}$. Experimental parameters: as in Figure 6. Simulation parameters: g = (2.0058, 2.0005, 1.9955), LW = (14, 10, 10) G, $A(^{14}N)$ = (12, 17, 12) MHz, $A(^{1}H)$ = (20, −10, −10) MHz, $A(^{17}O)$ = (11, 25, 25) MHz (weight 82%).

has been identified as an oxo bridge, $^{17}O_{Br}$ in the RNR **X** site [Fe(III)−O_{Br}−Fe(IV)].[14]

3.5.1.3. Composition and Structure of Relaxed X. The results of the present experiments establish that relaxed **X** contains one oxygen atom derived from O_2, present as an oxo bridge, identifying one bridging atom (Y) of Chart 1 as O_{Br}. In addition, it contains one oxygen atom derived from the solvent in the form of the hydroxyl bound to the Fe(III) ion. Thus, the composition of the inorganic core of relaxed **X** is shown to be [$(OH^-)Fe^{III}$)−O−Fe^{IV}]. As our measurements concur with the recent EXAFS study in implying that **X** exhibits the "diamond core" of Chart 1, this in turn requires that the second bridging atom (Z) of Chart 1 is protein-derived. This bridge is most plausibly assigned as a carboxyl oxygen; as has been discussed previously,[22] this would involve E238. With retention of the bridging carboxylate of Glu 115, this yields as the core of relaxed **X** the structure shown in Chart 2.

Chart 2

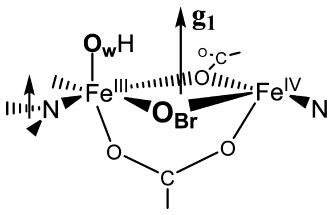

The same composition of the inorganic core of relaxed **X** (although without identification of the aqua ligand as a hydroxyl) was in fact first proposed by us in 1998. However, this conclusion was generally rejected, without addressing the evidence on which it was based, because it was thought to imply an Fe−Fe distance longer than the accepted value for the Fe−Fe distance, 2.51 Å. The recent revision of that distance to 2.78 Å[24] alleviates such concerns, although the basis for the difference between the earlier and latter EXAFs data still remains unclear.

4. CONCLUSIONS: THE STRUCTURE OF RELAXED X

The suite of advanced paramagnetic resonance techniques applied to **X** freeze-quenched at 4 s confirm the previously proposed composition of the inorganic core of **X**, and provide new insights into its structure. The present measurements have established the following conclusions:

(i) The ^{57}Fe and ^{14}N ENDOR spectra of **X**(WT) quenched at 42 ms and **X**(Y122F) quenched at 8−42 ms and 4 s all are identical, indicating that the properties of the [Fe_2, His_2] coordination center of **X** are unchanged by the Y122F mutation, and are invariant during relaxation as the quench delay increases.

(ii) ^{17}O ENDOR and quantitative EPR from **X** enriched separately with $H_2{}^{17}O$ and $^{17}O_2$(g), along with ^{1,2}H ENDOR, show that relaxed **X** contains one Fe(III)-bound hydroxide oxygen ($^{17}O_w$) derived from the solvent and one oxo bridge derived from O_2 gas ($^{17}O_{Br}$).

(iii) The hyperfine coupling to the second ^{17}O from $^{17}O_2$ is lost during the relaxation process, and there is no bridging ^{17}O from the enriched solvent. Thus, the inorganic core of relaxed **X** does *not* have a second inorganic oxygenic bridge, neither oxo nor hydroxo: its composition is [$(OH^-)Fe^{III}$−O−Fe^{IV}].

(iv) The geometric analysis of the ^{14}N ENDOR data, together with EXAFS measurements of the Fe−Fe distance, supports the view that **X** contains a "diamond-core"[35] Fe(III)/Fe(IV) center, Chart 1.

(v) One bridging ligand of the core of **X** (Chart 1, atom Y) is the oxo bridge (O_{Br}) derived from O_2 gas. Given the absence of a second inorganic oxygenic bridge (point iii), the second bridging ligand, Z, must be protein-derived, and is most plausibly assigned as a carboxyl oxygen from E238, yielding as the core of relaxed **X** the structure shown in Chart 2.

■ ASSOCIATED CONTENT

Supporting Information

The Supporting Information is available free of charge on the ACS Publications website at DOI: 10.1021/jacs.5b10763.

Figures showing the ^{57}Fe, ^{17}O, and ^{1}H ENDOR and EPR spectra (PDF)

■ AUTHOR INFORMATION

Corresponding Authors

*ped131@northwestern.edu
*stubbe@mit.edu
*bmh@northwestern.edu

Notes

The authors declare no competing financial interest.

■ ACKNOWLEDGMENTS

This work has been supported by the National Institutes of Health (Grants GM 111097 (B.M.H.) and GM 29595 (J.S.)). We thank Dr. Andrei Astashkin (University of Arizona) for insightful discussions of ENDOR/EPR protocols.

■ REFERENCES

(1) Eklund, H.; Uhlin, U.; Farnegardh, M.; Logan, D.; Nordlund, P. *Prog. Biophys. Mol. Biol.* **2001**, *77*, 177.
(2) Solomon, E. I.; Brunold, T. C.; Davis, M. I.; Kemsley, J. N.; Lee, S.-K.; Lehnert, N.; Neese, F.; Skulan, A. J.; Yang, Y.-S.; Zhou, J. *Chem. Rev.* **2000**, *100*, 235.
(3) Nordlund, P.; Eklund, H. *Curr. Opin. Struct. Biol.* **1995**, *5*, 758.
(4) Feig, A. L.; Lippard, S. J. *Chem. Rev.* **1994**, *94*, 759.

DOI: 10.1021/jacs.5b10763
J. Am. Chem. Soc. 2015, 137, 15558−15566

(5) Licht, S.; Stubbe, J. *Mechanistic Investigations of Ribonucleotide Reductases*; Elsevier: New York, 1999; Vol. 5.
(6) Stubbe, J.; Riggs-Gelasco, P. *Trends Biochem. Sci.* **1998**, *23*, 438.
(7) Stubbe, J.; van der Donk, W. A. *Chem. Rev.* **1998**, *98*, 705.
(8) Atkin, C. L.; Thelander, L.; Reichard, P.; Lang, G. *J. Biol. Chem.* **1973**, *248*, 7464.
(9) Sjoberg, B. M.; Reichard, P.; Graslund, A.; Ehrenberg, A. *J. Biol. Chem.* **1978**, *253*, 6863.
(10) Mitic, N.; Clay, M. D.; Saleh, L.; Bollinger, J. M.; Solomon, E. I. *J. Am. Chem. Soc.* **2007**, *129*, 9049.
(11) Riggs-Gelasco, P. J.; Shu, L.; Chen, S.; Burdi, D.; Huynh, B. H.; Que, L., Jr.; Stubbe, J. *J. Am. Chem. Soc.* **1998**, *120*, 849.
(12) Willems, J.-P.; Lee, H.-I.; Burdi, D.; Doan, P. E.; Stubbe, J.; Hoffman, B. M. *J. Am. Chem. Soc.* **1997**, *119*, 9816.
(13) Burdi, D.; Sturgeon, B. E.; Tong, W. H.; Stubbe, J.; Hoffman, B. M. *J. Am. Chem. Soc.* **1996**, *118*, 281.
(14) Burdi, D.; Willems, J.; Riggs-Gelasco, P.; Antholine, W.; Stubbe, J.; Hoffman, B. *J. Am. Chem. Soc.* **1998**, *120*, 12910.
(15) Ravi, N.; Bollinger, J. M., Jr.; Huynh, B. H.; Edmondson, D. E.; Stubbe, J. *J. Am. Chem. Soc.* **1994**, *116*, 8007.
(16) Bollinger, J. M., Jr.; Tong, W. H.; Ravi, N.; Huynh, B. H.; Edmondson, D. E.; Stubbe, J. *J. Am. Chem. Soc.* **1994**, *116*, 8024.
(17) Bollinger, J. M., Jr.; Edmondson, D. E.; Huynh, B. H.; Filley, J.; Norton, J. R.; Stubbe, J. *Science* **1991**, *253*, 292.
(18) Bollinger, J. M., Jr.; Tong, W. H.; Ravi, N.; Huynh, B. H.; Edmonson, D. E.; Stubbe, J. *J. Am. Chem. Soc.* **1994**, *116*, 8015.
(19) Sturgeon, B. E.; Burdi, D.; Chen, S.; Huynh, B. H.; Edmondson, D. E.; Stubbe, J.; Hoffman, B. M. *J. Am. Chem. Soc.* **1996**, *118*, 7551.
(20) Willems, J.-P.; Lee, H.-I.; Burdi, D.; Doan, P. E.; Stubbe, J.; Hoffman, B. M. In *ACS Advances in Chemistry*; Solomon, E., Hodgson, K., Eds.; American Chemical Society: Washington, DC, 1998; p 2.
(21) Han, W.-G.; Liu, T.; Lovell, T.; Noodleman, L. *Inorg. Chem.* **2006**, *45*, 8533.
(22) Han, W.-G.; Liu, T.; Lovell, T.; Noodleman, L. *J. Am. Chem. Soc.* **2005**, *127*, 15778.
(23) Shanmugam, M.; Doan, P. E.; Lees, N. S.; Stubbe, J.; Hoffman, B. M. *J. Am. Chem. Soc.* **2009**, *131*, 3370.
(24) Dassama, L. M.; Silakov, A.; Krest, C. M.; Calixto, J. C.; Krebs, C.; Bollinger, J. M., Jr.; Green, M. T. *J. Am. Chem. Soc.* **2013**, *135*, 16758.
(25) Davoust, C. E.; Doan, P. E.; Hoffman, B. M. *J. Magn. Reson., Ser. A* **1996**, *119*, 38.
(26) Zipse, H.; Artin, E.; Wnuk, S.; Lohman, G. J. S.; Martino, D.; Griffin, R. G.; Kacprzak, S.; Kaupp, M.; Hoffman, B.; Bennati, M.; Stubbe, J.; Lees, N. *J. Am. Chem. Soc.* **2009**, *131*, 200.
(27) Hoffman, B. M.; DeRose, V. J.; Doan, P. E.; Gurbiel, R. J.; Houseman, A. L. P.; Telser, J. *Biol. Magn. Reson.* **1993**, *13*, 151.
(28) Hoffman, B. M. *Acc. Chem. Res.* **2003**, *36*, 522.
(29) Hoffman, B. *Proc. Natl. Acad. Sci. U. S. A.* **2003**, *100*, 3575.
(30) Bencini, A.; Gatteschi, D. *EPR of Exchange Coupled Systems*; Dover Publications: New York, 2012.
(31) Doan, P. E.; Telser, J.; Barney, B. M.; Igarashi, R. Y.; Dean, D. R.; Seefeldt, L. C.; Hoffman, B. M. *J. Am. Chem. Soc.* **2011**, *133*, 17329.
(32) Scholes, C. P.; Lapidot, A.; Mascarenhas, R.; Inubushi, T.; Isaacson, R. A.; Feher, G. *J. Am. Chem. Soc.* **1982**, *104*, 2724.
(33) Logan, D. T.; Su, X. D.; Aberg, A.; Regnstrom, K.; Hajdu, J.; Eklund, H.; Nordlund, P. *Structure* **1996**, *4*, 1053.
(34) Nordlund, P.; Eklund, H. *J. Mol. Biol.* **1993**, *232*, 123.
(35) Xue, G.; Pokutsa, A.; Que, L. *J. Am. Chem. Soc.* **2011**, *133*, 16657 and references therein..
(36) Hoffman, B. M.; Gurbiel, R. J.; Werst, M. M.; Sivaraja, M. In *Advanced EPR. Applications in Biology and Biochemistry*; Hoff, A. J., Ed.; Elsevier: Amsterdam, 1989; p 541.
(37) Mathews, J.; Walker, R. L. *Mathematical Methods of Physics*; W. A. Benjamin, Inc.: New York, 1965.

DOI: 10.1021/jacs.5b10763
J. Am. Chem. Soc. 2015, 137, 15558−15566